

Antiphase Boundaries Constitute Fast Cation Diffusion Paths in SrTiO₃ Memristive Devices

Thomas Heisig,* Joe Kler, Hongchu Du, Christoph Baeumer, Felix Hensling, Maria Glöß, Marco Moors, Andrea Locatelli, Tevfik Onur Menteş, Francesca Genuzio, Joachim Mayer, Roger A. De Souza, and Regina Dittmann*

Resistive switching in transition metal oxide-based metal-insulator-metal structures relies on the reversible drift of ions under an applied electric field on the nanoscale. In such structures, the formation of conductive filaments is believed to be induced by the electric-field driven migration of oxygen anions, while the cation sublattice is often considered to be inactive. This simple mechanistic picture of the switching process is incomplete as both oxygen anions and metal cations have been previously identified as mobile species under device operation. Here, spectromicroscopic techniques combined with atomistic simulations to elucidate the diffusion and drift processes that take place in the resistive switching model material SrTiO₃ are used. It is demonstrated that the conductive filament in epitaxial SrTiO₃ devices is not homogenous but exhibits a complex microstructure. Specifically, the filament consists of a conductive Ti³⁺-rich region and insulating Sr-rich islands. Transmission electron microscopy shows that the Sr-rich islands emerge above Ruddlesden–Popper type antiphase boundaries. The role of these extended defects is clarified by molecular static and molecular dynamic simulations, which reveal that the Ruddlesden–Popper antiphase boundaries constitute diffusion fast-paths for Sr cations in the perovskites structure.


elements in next-generation nonvolatile memories,^[1–3] neuromorphic systems,^[4–8] analog computing^[9,10] as well as storage class memory^[11,12] applications. In contrast to conventional semiconductor memory devices, such as Flash or DRAM, that are based on manipulation of electronic charge, nanoionic memristive devices rely on the transport of ions.^[13] Such devices typically consist of a simple metal-insulator-metal structure that can be switched between high- and low-resistance states (HRS and LRS) through the application of an external electric field.^[14] For transition metal oxide-based devices it is commonly agreed that the switching process is caused by the drift of oxygen anions in the electric field, resulting in the creation of oxygen-vacancy rich filaments, also known as the valence change mechanism. Understanding the complex ionic and electronic transport processes under electric fields is therefore a prerequisite to further optimize device properties

and promote technological advances. However, owing to their nanoscale dimensions and the buried nature of the switching layer, conductive filaments are inherently difficult to locate and characterize. These difficulties are exacerbated by the extreme

1. Introduction

Due to their unique functionalities, nanoionic-based memristive devices have attracted considerable interest as the active

T. Heisig, Dr. C. Baeumer, Dr. F. Hensling, M. Glöß, Dr. M. Moors, Prof. R. Dittmann
Peter Gruenberg Institute 7
Forschungszentrum Juelich GmbH
52425 Juelich, Germany
E-mail: t.heisig@fz-juelich.de; r.dittmann@fz-juelich.de
T. Heisig, Dr. C. Baeumer, Dr. F. Hensling, M. Glöß, Dr. M. Moors, Prof. R. Dittmann
JARA-FIT
RWTH Aachen University
52056 Aachen, Germany

 The ORCID identification number(s) for the author(s) of this article can be found under <https://doi.org/10.1002/adfm.202004118>.

© 2020 The Authors. Published by Wiley-VCH GmbH. This is an open access article under the terms of the Creative Commons Attribution-NonCommercial-NoDerivs License, which permits use and distribution in any medium, provided the original work is properly cited, the use is non-commercial and no modifications or adaptations are made.

DOI: 10.1002/adfm.202004118

J. Kler, Prof. R. A. De Souza
Institute of Physical Chemistry
RWTH Aachen University
52056 Aachen, Germany
Dr. H. Du, Prof. J. Mayer
Ernst Ruska-Centre for Microscopy and Spectroscopy with Electrons
Forschungszentrum Juelich GmbH and RWTH Aachen University
52425 Juelich, Germany
Dr. H. Du, Prof. J. Mayer
Central Facility for Electron Microscopy
RWTH Aachen University
52074 Aachen, Germany
Dr. M. Moors
Department of Functional Surfaces
Leibniz-Institute of Surface Engineering (IOM)
Permoserstraße 15, 04318 Leipzig, Germany
Dr. A. Locatelli, Dr. T. O. Menteş, Dr. F. Genuzio
Elettra – Sincrotrone Trieste S.C.p.A.
S.S. 14 km – 163,5 in AREA Science Park, Basovizza, Trieste I-34149, Italy

conditions under which devices operate, namely high electric fields, high local temperatures, and fast switching times.^[15,16] Recent studies have revealed that besides the drift of oxygen anions, the cation sublattice also becomes mobile under these conditions and plays an important role in the switching process and device performance of two well-established valence change materials SrTiO₃^[17–21] and Ta₂O₅.^[22–25] In the case of SrTiO₃, especially the movement of Sr ions and the consequent precipitation of secondary phases was found to have a substantial impact on the device-retention and forming behavior.^[17,26,27] While the precipitation of a Sr-rich phase has been observed many times, the mechanistic details of this process remain unclear so far. Specifically, it is not yet known whether the precipitation occurs randomly or at preferential locations, whether the cations diffuse along the same path as the oxygen anions and if the process is electric field or thermodynamically driven.

In this study, spectromicroscopic characterization techniques are combined with molecular static and molecular dynamic simulations to investigate the ionic transport processes that lead to the resistive switching properties of the model valence-change material SrTiO₃. Because of its well-understood defect chemistry and structural properties, SrTiO₃ serves as an ideal material platform to examine and simulate ionic diffusion processes.^[28–30] Here, using laboratory-based UV as well as synchrotron based X-ray photoemission electron microscopy (PEEM), we find that the high temperatures generated during device operation significantly modify the anionic and cationic composition inside and in the surroundings of the conductive filament. The modified area is found to scale linearly with the used current compliance (CC). For higher currents we observe that cations become mobile and form precipitates at the SrTiO₃/top-electrode interface. Spectromicroscopic evidence combined with conductive atomic force microscopy (C-AFM) provides new insights into the microscopic structure of the filaments and into the retention stabilization effect of the Sr-rich precipitations. Importantly, scanning transmission electron microscopy (STEM) suggests that the cation diffusion occurs preferentially along Ruddlesden–Popper type antiphase boundaries (RP APB). Molecular static and molecular dynamic simulations confirm that RP APB provide a diffusion fast path by significantly lowering the Sr ion migration energy from 4.0 to 1.3 eV.

2. Results

To investigate the physical and chemical processes induced by the electroforming process in SrTiO₃ memristive devices, Pt/SrTiO₃/Nb:SrTiO₃ metal-insulator-metal structures were fabricated and electroformed with CC ranging from 7.5 to 50 mA. **Figure 1a** shows the electroforming process (i.e., the first switching process marked by the dashed lines) and switching characteristics of such devices. All devices exhibit an eight-wise switching polarity^[31] and could be set into the LRS by sweeping from 0 to nominally +4 V until the current compliance is reached, while sweeping to –4 V was used to reset the device into the HRS. All voltages were applied to the Pt top electrode. For devices formed and switched using different currents, it was observed that the CC has only a small effect on the device *I*–*V* characteristics and no influence on the HRS and

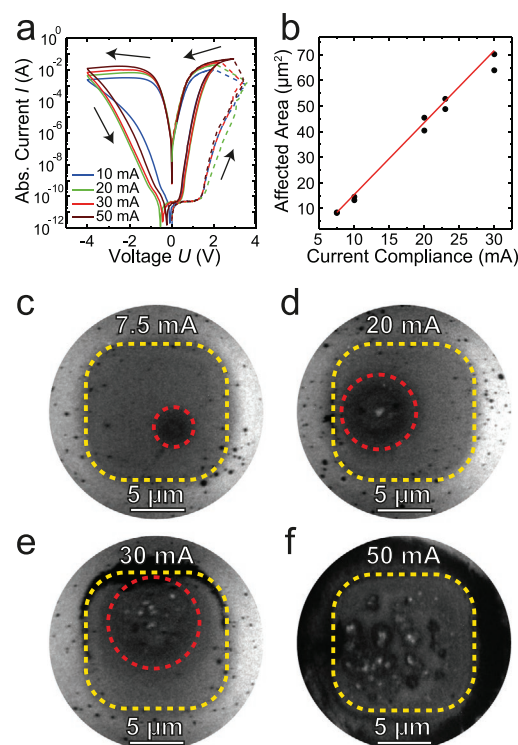


Figure 1. Change of filament size and structure with increasing forming current compliance. a) *I*–*V* curves of devices switched with current compliances from 10 to 50 mA. The dashed lines show the electroforming step. b) Affected area as a function of current compliance. c–f) Laboratory-based UV-PEEM images of electroformed and delaminated devices.

LRS states for read-out voltages below ± 0.5 V. The effect of the different CC on the endurance and variability is discussed in more detail in Figure S7 (Supporting Information). In order to study the chemical changes of the switched SrTiO₃ thin film, we used surface sensitive laboratory-based UV-PEEM; the Pt top-electrode was mechanically removed under ultra high vacuum (UHV) conditions directly before the analysis to prevent the reoxidation of the conductive filament. The former electrode area can easily be distinguished from the surrounding SrTiO₃ surface due to a remaining halo of thin Pt that formed during top-electrode evaporation through a shadow mask. For switched devices dark and bright contrasts are visible in parts of the electrode area, while virgin devices showed no such contrast. Figure 1b displays the estimated size of the affected area as a function of the CC extracted from work function contrast UV-PEEM images (see Figure 1c–f). For every CC at least two devices were investigated. The device switched with 7.5 mA exhibits a comparably small filament area of ≈ 10 μm^2 , visible as a dark spot inside the pad area. For $7.5 \text{ mA} \leq \text{CC} \leq 30 \text{ mA}$, the affected area increases linearly with the CC and an increasing number of additional bright spots with diameters of up to 500 nm emerged inside the affected area, suggesting that these modifications are caused by high local temperatures that arise during application of large currents. Devices switched with a CC above 30 mA exhibit affected areas that are larger than the top-electrode area and hence no estimation for the size of the affected area is given. Devices in both resistance states (LRS and

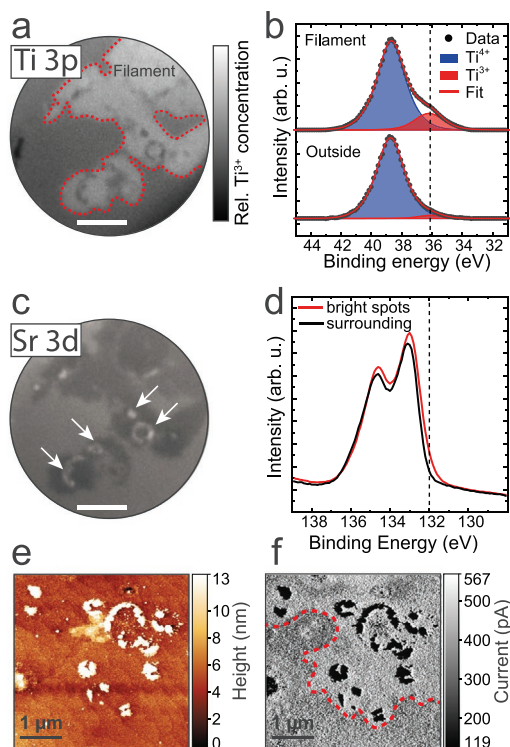


Figure 2. Microscopic filament investigation. a) X-PEEM image of the filament region acquired at a binding energy of 36.2 eV showing the Ti^{3+} concentration based on the Ti 3p core level spectrum (scale bar: 2 μm). b) Ti 3p spectra extracted from the filament and surrounding area. The dotted line indicates the selected binding energy in (a). c) XPEEM image based on the Sr 3d core level spectrum at 131.9 eV binding energy. d) Sr 3d spectra extracted from the bright spots (marked with white arrows in (c)) and the surrounding area. e) AFM image of a filament of a similar device and f) the corresponding C-AFM current map. The data in (a) and (b) have been published in parts in ref.[51].

HRS) have been investigated, but no apparent difference was visible. Figure S8 (Supporting Information) shows a side to side comparison of LRS and HRS devices. The dark contrast around the device in Figure 1f stems from platinum residues that were not removed during the delamination process (compare Figure S9 for further details, Supporting Information). Here we would like to note that while the observed affected areas are typical for epitaxial SrTiO_3 devices, they are considerably larger than filamentary structures in other ReRAM devices. We attribute this to the large currents that are required to switch SrTiO_3 .

In order to obtain spectroscopic information about the local filament composition, a similar sample was delaminated and analyzed with synchrotron-based X-PEEM. X-PEEM was employed to map the Ti 3p and Sr 3d core levels across a filament region formed with a current compliance of 50 mA. **Figure 2a** shows an energy filtered image of the filament obtained at an electron energy of $E_{\text{bin}} = 36.2$ eV corresponding to the feature in the Ti 3p core level spectrum that we attribute to Ti^{3+} . A Ti^{3+} rich area appears as a bright region of irregular shape surrounded by a Ti^{4+} matrix (red dotted line). Inside the Ti^{3+} rich area, small dark spots are visible: they reveal that the filament is not homogeneous but is heterogeneously structured at submicrometer lengths. The corresponding Ti 3p XPS spectra

of the filament and the surrounding region are presented in **Figure 2b**. We find that the filament consists of up to 30% Ti^{3+} , while the surrounding area is composed almost entirely of Ti^{4+} . The high proportion of Ti^{3+} is attributed to heavy reduction of the matrix and thus indicates that a large amount of oxygen vacancies is present. The energy filtered image of the Sr 3d core level ($E_{\text{bin}} = 131.9$ eV) and the corresponding spectra are displayed in **Figure 2c,d**. The image shows that the Ti^{3+} rich region observed in **Figure 2a** is slightly Sr-deficient in comparison with regions outside of the filament. Inside the filament several features can be identified as bright spots (marked by white arrows) that coincide with the dark spots observed in the Ti 3p core level image. The spectrum extracted from the bright spots is shifted to lower binding energies in comparison to the reference spectrum. This suggests that an additional low binding energy component is present in these regions. A similar spectral shift has been reported in literature and was attributed to the formation of Sr_{Ti} antisite defects.^[18] To investigate the morphology and local electrical properties of such a filament, C-AFM was performed on a filament region after it was located using PEEM (see **Figure 2e,f**). The topographic image shows the well-known unit cell step terrace structure of an epitaxial SrTiO_3 film as well as islands that are up to 13 nm high. The larger islands often exhibit a characteristic ring-shape morphology, also observed in the PEEM data of **Figure 2a,c**. These islands were only observed in electroformed devices and were not present in virgin devices. In the conductivity map, just as in the X-PEEM images, three different regions can be distinguished. The highly insulating islands are surrounded by a widespread conductive region (highlighted by the red dotted line) and a region with medium conductivity farther away from the islands.

To overcome a common limitation of X-PEEM and AFM, that is, low or no sensitivity to the buried layers, we employed STEM and studied a filament in cross-section. For this, a lamella was cut across the filament presented in **Figure 2e** including parts of the islands that emerged during the electroforming process. **Figure 3a** displays a high-resolution dark-field (DF) STEM image of the SrTiO_3/Pt interface where an island was located. The film exhibits for the most part an epitaxial crystal quality, which is only disrupted by a RP APB located directly beneath and perpendicular to the precipitate.^[32,33] The RP APB consists of one vertical [010] and two horizontal [100] planes. A detailed description of the APB is presented in **Figure S1** (Supporting Information).^[34] **Figure 3b** shows a high angle annular dark-field (HAADF) STEM image of the area marked with a white box in **Figure 3a**, which clearly resolves that the SrTiO_3 lattices on both sides of the APB are displaced relative to each other by $a/2[111]$ (the z component is along the projection direction and therefore is not visible) and, with the intermediate TiO_2 plane missing, thereby result in two adjacent SrO atomic planes. Energy dispersive X-Ray (EDX) mapping was performed to study the elemental distribution across the filament section (see **Figure 3c–f**). The Pt-M α map indicates no measurable diffusion of Pt into the SrTiO_3 layer while the O-K, Sr-L α , and Ti-K α maps show a weak signal in the Pt layer. This could either indicate that small amounts of SrTiO_3 have diffused into the Pt layer or that an inelastic scattering of primary electrons in the much denser Pt layer induces the emission of characteristic X-rays in the SrTiO_3 layer through collisions with secondary

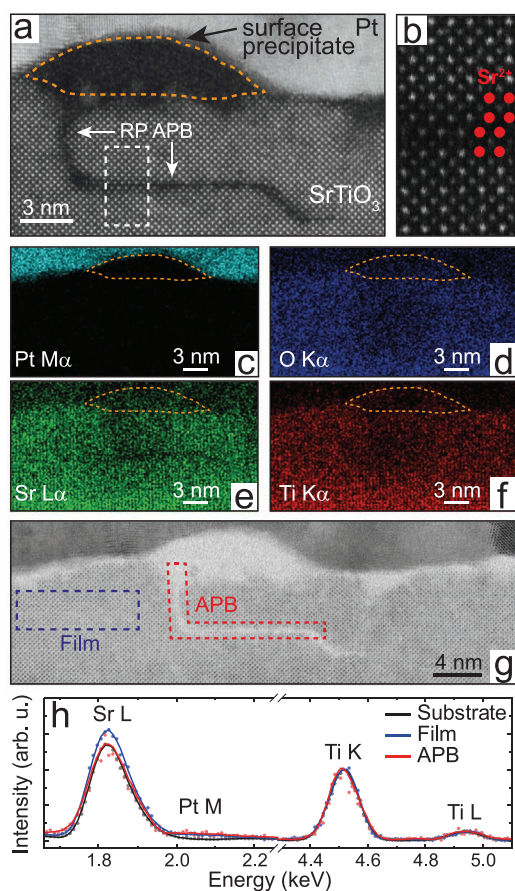


Figure 3. TEM filament investigation. a) DF-STEM image of the filament cross-section and b) HAADF image of the magnified part of the white box in (a). c–f) Elemental maps acquired by EDX for: c) Pt $M\alpha$, d) O $K\alpha$, e) Sr $L\alpha$, and f) Ti $K\alpha$. g) ABF image of the same region. EDX spectra of the thin film from 0 to 20 keV were summed from regions of interest located at the RP APB and close to the top electrode (Film) to enhance the signal-to-noise ratio. h) Smoothed (solid lines) spectra of the Sr-L and Ti-K lines normalized to the Ti-K peak.

electrons. Importantly, the Sr- $K\alpha$ map shows a distinct Sr depletion in the vicinity of the RP APB. This is unexpected, because the double SrO plane structure of the RP APB should be considerably richer in Sr than the bulk.^[35] To quantify the cation ratio around the APB and the thin film stoichiometry, atomic Sr/Ti ratios were determined from EDX spectra extracted from regions marked in Figure 3g using the substrate as an internal standard for calibration.^[19] The increased intensity of the Sr-L line reveals a $(5 \pm 2)\%$ Sr enrichment in the thin film compared to the substrate (see Figure 3h), which is consistent with the expected stoichiometry based on the pulsed laser deposition (PLD) growth rate and laser fluence.^[36,37] The Sr excess is likely to be incorporated into the thin film as randomly distributed small RP faults.^[32,37–39] Another possibility for the accommodation of the Sr excess is the presence of Ti vacancies.^[40] In contrast to the as-grown film, the stoichiometry of the area surrounding the RP APB (marked by the red dashed-line in Figure 3g) shows a cation ratio similar to the substrate. This indicates that, during the electroforming process, the Sr excess that was incorporated into the film during growth precipitates out of the thin film

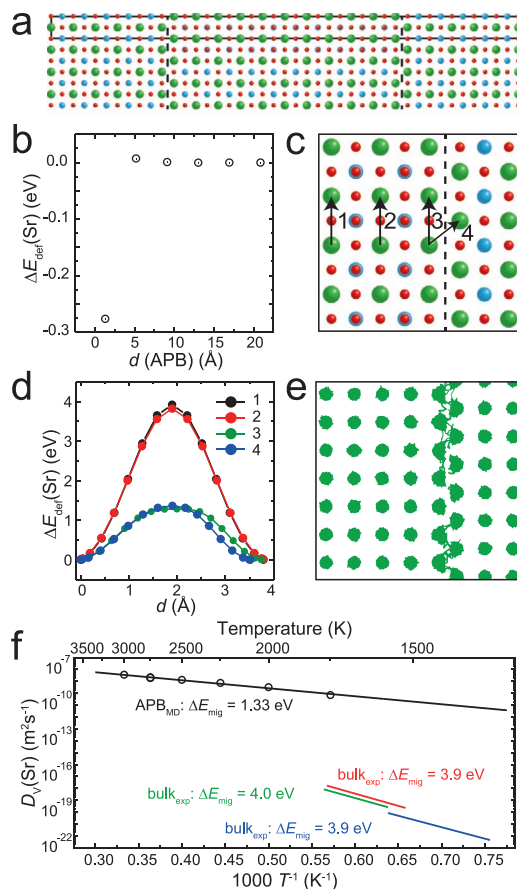


Figure 4. Static and molecular dynamics simulations of Sr vacancy behavior at RP defects. a) Illustration of the $Sr_{11}Ti_{10}O_{31}$ unit cell (solid black line) used in the atomistic simulations. Sr in green, Ti in blue, and O in red. The RP faults are marked by dashed black lines. b) Defect formation energy of an Sr vacancy as a function of distance to the APB. c) Magnified part of the unit cell, with the simulated migration path indicated schematically by black arrows. d) Strontium migration energies for the individual migration paths. e) Molecular dynamic trajectories of Sr cations at $T = 2000$ K. f) Diffusion coefficients of strontium vacancies along the APB obtained from molecular dynamic simulations (black) and experimental values in bulk $SrTiO_3$ by Meyer et al.^[42] (red) and Gömann et al.^[44] (blue and green) as a function of (reciprocal) temperature.

around RP APB. The annular bright field STEM image displayed in Figure 3g reveals that the material of the surface precipitate appears to be amorphous. Poor signal-to-noise ratio arising from less material and from overlapping Pt- $M\alpha$ and Sr- $L\alpha$ emission lines hinder a quantification of the precipitate stoichiometry in this area. However, from Figure 3f it is evident that the precipitate contains Ti, which suggests that Ti is mobile in both the film and the precipitate during electroforming.

Based on the findings that RP APB might act as diffusion fast path for cation diffusion, molecular static, and molecular dynamic simulations were performed. A high-order ($n = 10$) RP phase ($Sr_{11}Ti_{10}O_{31}$, Figure 4a) was used as a model system to examine cation transport in RP APB. This selection is motivated because such a RP phase exhibits not only the APB but also an extended bulk phase.^[41] First, the defect formation energy of a strontium vacancy was calculated for different lattice sites in the simulation cell (Figure 4b). Relative to the value in the

perovskite bulk, the defect formation energy is lower for the site located within the APB ($\Delta E \approx -0.28$ eV), i.e., the energetically most stable position for Sr vacancies is located within the APB. To gain insights into the migration processes of Sr ions, nudged-elastic band simulations were performed to determine the activation energy of different migration paths. Figure 4c shows selected migration paths, while the corresponding energy profiles are presented in Figure 4d. The migration paths in the perovskite type bulk phase (paths 1 and 2) have a high migration barrier of 4.0 eV, which is consistent with values obtained experimentally and computationally for SrTiO₃.^[42–45] The two possible migration paths (paths 3 and 4) in the double SrO plane structure of the RP APB have a significantly lower migration barrier of 1.3 eV, comparable to the migration barrier (obtained with these potentials) of Sr vacancy migration in rock-salt-type SrO. Based on the findings of the lowered migration barrier in the RP APB, molecular dynamics (MD) simulations of the high-order RP phase was carried out, with 1% cation vacancies equally distributed between the bulk phase and the RP APB. The trajectories of the Sr cations (Figure 4e) show that the cations only move in the double SrO plane structure RP APB and remain immobile in the bulk perovskite phase (at these simulation temperatures and for these simulation times). A closer look at the cation trajectories reveals that the cations move along the two same migration paths calculated to have a lowered migration barrier in the static lattice simulations. The obtained diffusion coefficients for Sr migration in RP APB for different temperatures yield a migration enthalpy of 1.3 eV (see Figure 4f), which compares extremely well with the static migration barriers in the RP APB. Since Sr cations did not execute any jumps in the bulk phase (owing to the high migration barrier of 4.0 eV), no diffusion coefficients for Sr ions outside the APB could be determined from the MD simulations. To estimate the difference, we compare in Figure 4f our strontium-vacancy diffusion coefficients for the APB with experimental data determined for single-crystal SrTiO₃ by Meyer et al.^[42] and Gömann et al.^[44] We contend that this is a valid comparison, since in a previous paper,^[46] we demonstrated that this set of pair potentials yields oxygen-vacancy diffusion coefficients in SrTiO₃ that are in excellent agreement with experiment,^[47] both in terms of activation enthalpy and absolute magnitude. Hence, we expect that, at temperatures below $T = 1273$ K, strontium vacancies will be ten or more orders of magnitude more mobile in the APB than in the bulk SrTiO₃ perovskite.

3. Discussion and Conclusions

The data obtained from X-PEEM, AFM, and STEM analysis reveal that the forming process in Pt/SrTiO₃/Nb:SrTiO₃ resistive switching devices causes the formation of islands at the Pt/SrTiO₃ interface. While a depth-resolved quantitative assessment of the island stoichiometry is not possible, we qualitatively find that the islands are rich in Sr, which is evidenced by a depletion of Sr underneath the island (Figure 3e) and by a decreased Ti signal from the island surface in the Ti 3p X-PEEM image (see Figure S3, Supporting Information). This observation is in good agreement with the work of Rahmati et al. who reported the formation of Sr-rich islands after high temperature

annealing of Nb:SrTiO₃ under oxygen atmosphere.^[48] The authors proposed that, in Sr-rich perovskite-type islands, the Sr excess is established through the formation of Sr_{Ti}' antisite defects and V_O'' counter defects. This is in accordance with the low binding component that is present in the Sr 3d core level spectrum of the island regions (Figure 3d), which we attribute to Sr_{Ti}' antisite defects.^[18]

Based on our PEEM measurements, we could determine that the area where precipitates have formed is directly proportional to the used CC. While the electric field strength is almost identical in all cases, the power dissipation and hence the Joule heating is greatly increasing with increasing CC according to: $P \approx I^2 \cdot R$ (where P is the power converted to thermal energy, I is the current, and R is the device resistance). This suggests that the island formation is a temperature accelerated but thermodynamically driven process rather than an ionic drift under the electric field. Considering the electric field direction during the forming step, a positive bias applied to the top electrode, one would assume that Sr cations are driven away from the top interface to the bottom. However, due to the densely packed crystal structure of SrTiO₃ and the epitaxial nature of the interface, Sr ions cannot be accommodated at the bottom interface. In contrast, at the top interface Sr can leave the lattice forming an Sr-rich secondary phase by deforming the metal electrode.^[18] Importantly, these results illustrate that the underlying driving forces that lead to anionic and cationic motion are different in nature. While the oxygen anion redistribution during the switching process is reliant on the electric field direction rather than being thermodynamically driven,^[49] it is the opposite case for the cation motion.

Unexpectedly, it was found that the LRS resistance does not scale with the CC within the here investigated current range, in contrast to the affected area that was determined by PEEM (Figure 1b). This implies that the area of the conductive filament is smaller than the affected area, as a larger filament should also increase the conductance of the device. Therefore, it is assumed that the initial electroforming step, where the highest electric fields are reached, determines the filament size and oxygen-vacancy concentration. In contrast the current limit controls the temperature development and hence the area in which cation motion can occur. From the X-PEEM and C-AFM measurements it is demonstrated that the Ti³⁺-rich region exhibits a high conductivity, while the Sr-rich islands are insulating. Recently, we could attribute the Ti³⁺ states to the presence of filament rich in oxygen vacancies and explain the resistance change between HRS and LRS through the modulation of the Schottky barrier at the top-electrode/SrTiO₃ interface.^[50,51] In contrast, the Sr-rich islands do not contribute to the resistance change of the device but are emerging during the electroforming step due to the high local temperatures that are present in the vicinity of the filament. Nevertheless, in a previous paper we demonstrated that the islands play a crucial role for improving the device retention by acting as oxygen diffusion barrier and thus stabilizing the LRS (see Figures S4 and S5, Supporting Information).^[17]

The important question remains if the islands are formed at random locations or if their position is predetermined. As visualized by STEM the location of the precipitates is connected to the position of vertical RP APB, suggesting that such

faults either can act as nucleation point or facilitate the phase formation by acting as a diffusion fast path. This question is answered by the molecular static simulations that show that the Sr migration barrier is considerably decreased along (1.3 eV) and across (1.4 eV) the RP APB in comparison to the bulk diffusion (4 eV). These findings are in good agreement with the experimentally determined values for the Sr migration barrier in bulk SrTiO₃.^[42,44] Furthermore, the molecular dynamics simulation demonstrates that Sr cations indeed move along the RP APB. Upon comparison of the Sr diffusion coefficient obtained by molecular dynamic simulations with experimentally determined Sr bulk diffusion coefficients, we conclude that diffusion along APB is orders of magnitude faster.

Finally, the characteristic ring shape of the precipitates (see Figure 2e) can be explained by considering the formation mechanism of RP APB in PLD grown thin films. During the growth of a Sr-rich thin film the surface is progressively enriched with SrO until it is completely covered by a monolayer of SrO.^[32] Any additional Sr excess then leads to the formation of 1 u.c. high SrO islands in a rock-salt like structure, which results in the creation of horizontal and vertical RP APB (see Figure 3a). Specifically, the vertical RP APB are located at the border of the growth induced SrO islands.^[32] As a result, the precipitates possess a ring like shape as they follow the contour of the APB.

In conclusion, here we have experimentally and theoretically verified that Sr diffusion takes place during resistive switching of epitaxial SrTiO₃ devices along Ruddlesden–Popper type antiphase boundaries. Our results reveal that the significantly decreased Sr ion migration energy along the APB results in the formation of Sr-rich islands above these defects. As visualized by means of STEM and EDX, the formation of Sr-rich islands goes along with a depletion of Sr in the vicinity of RP APB. The cation diffusion was determined to be predominantly caused by switching induced Joule heating rather than a drift under the applied electric field. While the findings in this paper cannot be directly transferred to technology relevant nanoscale ReRAM devices, they demonstrate the importance of extended defects for the functionality of mixed ionic-electronic devices and present a promising approach to improve their performance and long-term stability through defect engineering. Beyond the case of SrTiO₃, we believe that these results are of general importance for A-site rich A^{II}B^{IV}O₃ and A^{III}B^{III}O₃ perovskites, due to their tendency of forming Ruddlesden–Popper faults.

4. Experimental Section

Sample Fabrication of SrTiO₃ Memory Cells: A 20 nm single-crystalline nominally undoped SrTiO₃ thin film with an excess of Sr of ≈4% was fabricated by means of pulsed laser deposition on a 0.5 wt% Nb:SrTiO₃ substrate (CrysTec GmbH, Germany). The single-crystalline SrTiO₃ target was ablated by a KrF excimer laser ($\lambda = 248$ nm) with a repetition rate of 5 Hz and a spot size of 2 mm² at a target-to-substrate distance of 44 mm. The laser fluence was 0.77 J cm⁻². The sample was grown in an oxygen atmosphere of 0.1 mbar at a substrate temperature of 800 °C. Film growth was monitored with reflection high-energy electron diffraction. For the top electrodes, an 80 nm thick Pt layer was evaporated through a shadow mask to give electrodes with a size of 12 × 12 μm².

Top-Electrode Delamination: For spectromicroscopic and topographic analysis, the top-electrodes were delaminated under ultrahigh vacuum

conditions ($p < 10^{-8}$ mbar) with an adhesive copper tape after electron beam evaporation of a homogeneous 80 nm Pt layer onto the entire sample. The delaminated sample was transferred into the PEEM and AFM chambers under ultrahigh vacuum conditions.

Electrical Characterization: For electrical characterization, the Pt electrodes were contacted with tungsten whisker probes. The Nb:SrTiO₃ substrate served as an electrically grounded bottom electrode and was contacted by Al wire bonding. *I–V* sweeps were performed with a Keithley 2611A SourceMeter. The different sweeps were performed using the following voltage cycles: 0 V to positive voltages (maximum +4 V) for forming and set and 0 V to negative voltages (maximum –4 V) for reset. The step size was 20 mV and the holding time before measurement was 5 ms, resulting in a sweep rate of ≈0.54 V s⁻¹; the current compliance for the forming step and the set process varied between 7.5 and 50 mA. During the reset sweeps no current compliance was necessary.

Transmission Electron Microscopy: Cross-sectional lamellae of the devices were prepared by focus ion beam (FIB) using a FEI Helios NanoLab 400S (FEI Company, Hillsboro, OR). The lamellae were further thinned and finally cleaned by a Fischione Nanomill 1040 system (E.A. Fischione Instruments, Inc., Export, PA) with Ar ion beam at 900 and 500 V acceleration voltages, respectively. The high angle annular dark-field (HAADF)-STEM images and EDX spectra were recorded at 200 kV acceleration voltages with a beam semiconvergence angle of 25 mrad and an inner collection angle of 67 mrad of the HAADF detector with an FEI Titan 80-200 ChemiSTEM microscope.^[52]

Atomistic and Molecular Dynamic Simulations: Antiphase boundaries were modeled with classical methods using empirical pair potentials derived by Pedone et al.^[53]

$$V_{ij} = \frac{z_i z_j e^2}{r} + D_{ij} \left(\left(1 - e^{-a_j(r-r_0)} \right)^2 - 1 \right) + \frac{C_{ij}}{r^{12}} \quad (1)$$

The first term describes the long-range Coulomb interactions, the second term describes short-range interactions (Morse function) and the third term is a repulsive term that prevents the ions approaching each other too closely in molecular dynamics simulations. The parameters are shown in Table 1.

These potentials were initially derived for modeling glassy materials,^[53] but they also proved to reproduce properties of crystalline SrTiO₃. Waldow and De Souza used these potentials to successfully describe the oxygen diffusion in bulk STO and along grain boundaries in STO.^[46] In this study, antiphase boundaries were modeled using the Ruddlesden–Popper phase Sr₁₁Ti₁₀O₃₁. A 12 × 12 × 1 supercell containing 14976 ions (Sr₃₁₆₈Ti₂₈₈₀O₈₉₂₈) containing two parallel antiphase boundaries. The LAMMPS (Large-scale atomic/molecular massively parallel simulator)^[54] code was used to perform the Nudged-elastic band calculation and the MD simulations. The MD simulations were performed within the *NpT* ensemble with constant number of ions *N*, pressure *p*, and temperature *T*. 1% Sr vacancies were introduced in the supercell, equally distributed between the bulk phase and the antiphase boundaries, charge neutrality was accomplished by lowering *z*_O. For each temperature, the simulation cell was first equilibrated for 300 ps and then the main simulation was run for at least 500 ps to produce data.

Atomic Force Microscopy: The combined AFM/C-AFM measurements were performed using an Omicron VT-SPM system operating at room temperature under UHV conditions. The detection of the local surface conductance was achieved using silicon cantilevers with a boron doped

Table 1. Employed empirical pair potential parameters, derived by Pedone et al.^[53]

Pair	<i>D</i> _{<i>ij</i>} [meV]	<i>a</i> _{<i>ij</i>} [Å ⁻¹]	<i>r</i> ₀ [Å]	<i>C</i> _{<i>ij</i>} [eV Å ¹²]
Sr ^{+1,2} –O ^{-1,2}	19.623	1.8860	3.32 833	3.0
Ti ^{+2,4} –O ^{-1,2}	24.235	2.2547	2.70 894	1.0
O ^{-1,2} –O ^{-1,2}	42.395	1.3793	3.61 870	22.0

polycrystalline diamond coating. The cantilever tips had a nominal radius of less than 150 nm and a spring constant of 25 N m⁻¹ (AppNano, DD-ACTA-10). The measurements were performed with a Set-Force of 2 nN and a sample bias of 1 V. The noise level was estimated on a homogeneous region of a scan to be $\approx \pm 30$ pA, being significantly lower than the difference between the conductive and virgin region ($\Delta I > 85$ pA).

Photoemission Electron Spectromicroscopy: The XPEEM experiments were performed using the SPELEEM microscope operating at the Nanospectroscopy beamline at Elettra synchrotron laboratory, Trieste, Italy.^[55] Core level photoemission spectra were extracted from the resulting image stack in different regions of interest and a Shirley background was subtracted. The fitting of the core level photoelectron spectra was performed with CasaXPS Version 2.3.16.^[56] The components were constrained to have the same peak position and width for each fit. False color maps were created by summing up several images within each peak and dividing the resulting images.

Supporting Information

Supporting Information is available from the Wiley Online Library or from the author.

Acknowledgements

Funding from the DFG (German Science Foundation) within the collaborative research center SFB 917 “Nanoswitches” is gratefully acknowledged. T.H., C.B., and R.D. also acknowledge funding from the W2/W3 program of the Helmholtz association. C.B. received funding from the European Union’s Horizon 2020 research and innovation program under the Marie Skłodowska-Curie Grant Agreement No. 796142. The authors thank Maximilian Kruth for the TEM sample preparation by FIB. The authors thank Carsten Funck and Sebastian Siegel for the simulation and for the fruitful discussions of the manuscript.

Open access funding enabled and organized by Projekt DEAL.

Conflict of Interest

The authors declare no conflict of interest.

Author Contributions

T.H., C.B., and R.D. conceived and designed the experiments. T.H. and C.B. fabricated the samples. T.H. and C.B. performed the UV based PEEM experiments. J.K. and R.A.D.S. performed and designed the molecular static and molecular dynamic simulations. H.D. carried out the TEM imaging. M.G. and M.M. performed the CAFM measurements. C.B., A.L., T.O.M., and F.G. conducted the X-PEEM experiments. T.H., F.H., J.K., C.B., R.A.D.S., and R.D. evaluated and interpreted the results. J.M., R.A.D.S., and R.D. supervised the research. T.H. wrote the manuscript supported by important discussions with C.B., R.A.D.S., and R.D. and contributions from all authors.

Keywords

diffusion, resistive switching, Ruddlesden–Popper, SrTiO₃, STEM

Received: May 12, 2020
Revised: August 24, 2020
Published online:

- [1] R. Waser, R. Dittmann, C. Staikov, K. Szot, *Adv. Mater.* **2009**, *21*, 2632.
- [2] M. Wang, S. Cai, C. Pan, C. Wang, X. Lian, Y. Zhuo, K. Xu, T. Cao, X. Pan, B. Wang, S. J. Liang, J. J. Yang, P. Wang, F. Miao, *Nat. Electron.* **2018**, *1*, 130.
- [3] M. J. Lee, C. B. Lee, D. Lee, S. R. Lee, M. Chang, J. H. Hur, Y. B. Kim, C. J. Kim, D. H. Seo, S. Seo, U. I. Chung, I. K. Yoo, K. Kim, *Nat. Mater.* **2011**, *10*, 625.
- [4] M. Prezioso, F. Merrikh-Bayat, B. D. Hoskins, G. C. Adam, K. K. Likharev, D. B. Strukov, *Nature* **2015**, *521*, 61.
- [5] S. H. Jo, T. Chang, I. Ebong, B. B. Bhadviya, P. Mazumder, W. Lu, *Nano Lett.* **2010**, *10*, 1297.
- [6] Z. Wang, S. Joshi, S. Savel'Ev, W. Song, R. Midya, Y. Li, M. Rao, P. Yan, S. Asapu, Y. Zhuo, H. Jiang, P. Lin, C. Li, J. H. Yoon, N. K. Upadhyay, J. Zhang, M. Hu, J. P. Strachan, M. Barnell, Q. Wu, H. Wu, R. S. Williams, Q. Xia, J. J. Yang, *Nat. Electron.* **2018**, *1*, 137.
- [7] M. A. Zidan, J. P. Strachan, W. D. Lu, *Nat. Electron.* **2018**, *1*, 22.
- [8] J. Xiong, R. Yang, J. Shaibo, H. M. Huang, H. K. He, W. Zhou, X. Guo, *Adv. Funct. Mater.* **2019**, *29*, 1807316.
- [9] F. Cüppers, S. Menzel, C. Bengel, A. Hardtdegen, M. Von Witzleben, U. Böttger, R. Waser, S. Hoffmann-Eifert, *APL Mater.* **2019**, *7*, 091105.
- [10] C. Li, M. Hu, Y. Li, H. Jiang, N. Ge, E. Montgomery, J. Zhang, W. Song, N. Dávila, C. E. Graves, Z. Li, J. P. Strachan, P. Lin, Z. Wang, M. Barnell, Q. Wu, R. S. Williams, J. J. Yang, Q. Xia, *Nat. Electron.* **2018**, *1*, 52.
- [11] S. R. Lee, Y. B. Kim, M. Chang, K. M. Kim, C. B. Lee, J. H. Hur, G. S. Park, D. Lee, M. J. Lee, C. J. Kim, U. I. Chung, I. K. Yoo, K. Kim, in *Dig. Tech. Pap. – Symp. VLSI Technol.*, IEEE, Piscataway, NJ **2012**, pp. 71–72.
- [12] C. Hsu, I. Wang, C. Lo, M. Chiang, W. Jang, in *Dig. Tech. Pap. — Symp. VLSI Circuits*, IEEE, Piscataway, NJ **2013**, p. 166.
- [13] X. Zhu, W. Su, Y. Liu, B. Hu, L. Pan, W. Lu, J. Zhang, R. W. Li, *Adv. Mater.* **2012**, *24*, 3941.
- [14] R. Waser, M. Aono, *Nanosci. Technol.* **2009**, *6*, 158.
- [15] A. C. Torrezan, J. P. Strachan, G. Medeiros-Ribeiro, R. S. Williams, *Nanotechnology* **2011**, *22*, 485203.
- [16] C. Lenser, M. Patt, S. Menzel, A. Köhl, C. Wiemann, C. M. Schneider, R. Waser, R. Dittmann, *Adv. Funct. Mater.* **2014**, *24*, 4466.
- [17] C. Baeumer, C. Schmitz, A. H. H. Ramadan, H. Du, K. Skaja, V. Feyer, P. Muller, B. Arndt, C. L. Jia, J. Mayer, R. A. De Souza, C. Michael Schneider, R. Waser, R. Dittmann, *Nat. Commun.* **2015**, *6*, 8610.
- [18] C. Lenser, A. Koehl, I. Slipukhina, H. Du, M. Patt, V. Feyer, C. M. Schneider, M. Lezaic, R. Waser, R. Dittmann, *Adv. Funct. Mater.* **2015**, *25*, 6360.
- [19] H. Du, C. L. Jia, A. Koehl, J. Barthel, R. Dittmann, R. Waser, J. Mayer, *Chem. Mater.* **2017**, *29*, 3164.
- [20] D. Kwon, S. Lee, C. S. Kang, Y. S. Choi, S. J. Kang, H. L. Cho, W. Sohn, J. Jo, S. Lee, K. H. Oh, T. W. Noh, R. A. De Souza, M. Martin, M. Kim, *Adv. Mater.* **2019**, *31*, 1970205.
- [21] Y. Su Kim, J. Kim, M. Jee Yoon, C. Hee Sohn, S. Buhm Lee, D. Lee, B. Chul Jeon, H. Keun Yoo, T. Won Noh, A. Bostwick, E. Rotenberg, J. Yu, S. Don Bu, B. Simon Mun, *Appl. Phys. Lett.* **2014**, *104*, 013501.
- [22] J. P. Strachan, G. Medeiros-Ribeiro, J. J. Yang, M. X. Zhang, F. Miao, I. Goldfarb, M. Holt, V. Rose, R. S. Williams, *Appl. Phys. Lett.* **2011**, *98*, 242114.
- [23] Y. Ma, J. M. Goodwill, D. Li, D. A. Cullen, J. D. Poplawsky, K. L. More, J. A. Bain, M. Skowronski, *Adv. Electron. Mater.* **2019**, *5*, 1800954.

- [24] Y. Ma, D. Li, A. A. Herzing, D. A. Cullen, B. T. Sneed, K. L. More, N. T. Nuhfer, J. A. Bain, M. Skowronski, *ACS Appl. Mater. Interfaces* **2018**, *10*, 23187.
- [25] A. Wedig, M. Luebben, D. Y. Cho, M. Moors, K. Skaja, V. Rana, T. Hasegawa, K. K. Adepalli, B. Yildiz, R. Waser, I. Valov, *Nat. Nanotechnol.* **2016**, *11*, 67.
- [26] F. V. E. Hensling, T. Heisig, N. Raab, C. Baeumer, R. Dittmann, *Solid State Ionics* **2018**, *325*, 247.
- [27] C. Baeumer, N. Raab, T. Menke, C. Schmitz, R. Rosezin, P. Müller, M. Andrä, V. Feyer, R. Bruchhaus, F. Gunkel, C. M. Schneider, R. Waser, R. Dittmann, *Nanoscale* **2016**, *8*, 13967.
- [28] R. A. De Souza, *Adv. Funct. Mater.* **2015**, *25*, 6326.
- [29] T. Shi, Y. Chen, X. Guo, *Prog. Mater. Sci.* **2016**, *80*, 77.
- [30] R. Moos, K. H. Hardtl, *J. Am. Ceram. Soc.* **2005**, *80*, 2549.
- [31] R. Muenstermann, T. Menke, R. Dittmann, R. Waser, *Adv. Mater.* **2010**, *22*, 4819.
- [32] C. Xu, H. Du, A. J. H. Van Der Torren, J. Aarts, C. L. Jia, R. Dittmann, *Sci. Rep.* **2016**, *6*, 38296.
- [33] S. N. Ruddlesden, P. Popper, *Acta Crystallogr.* **1958**, *11*, 54.
- [34] W. Y. Wang, Y. L. Tang, Y. L. Zhu, J. Suriyaprakash, Y. B. Xu, Y. Liu, B. Gao, S. W. Cheong, X. L. Ma, *Sci. Rep.* **2015**, *5*, 16097.
- [35] F. V. E. Hensling, H. Du, N. Raab, C. L. Jia, J. Mayer, R. Dittmann, *APL Mater.* **2019**, *7*, 101127.
- [36] N. Raab, C. Bäumer, R. Dittmann, *AIP Adv.* **2015**, *5*, 047150.
- [37] C. Xu, S. Wicklein, A. Sambri, S. Amoroso, M. Moors, R. Dittmann, *J. Phys. D: Appl. Phys.* **2014**, *47*, 034009.
- [38] E. Breckenfeld, R. Wilson, J. Karthik, A. R. Damodaran, D. G. Cahill, L. W. Martin, *Chem. Mater.* **2012**, *24*, 331.
- [39] T. Ohnishi, K. Shibuya, T. Yamamoto, M. Lippmaa, *J. Appl. Phys.* **2008**, *103*, 103703.
- [40] D. J. Keeble, S. Wicklein, L. Jin, C. L. Jia, W. Egger, R. Dittmann, *Phys. Rev. B: Condens. Matter Mater. Phys.* **2013**, *87*, 195409.
- [41] A. H. H. Ramadan, N. L. Allan, R. A. De Souza, *J. Am. Ceram. Soc.* **2013**, *96*, 2316.
- [42] R. Meyer, R. Waser, J. Helmbold, G. Borchardt, *Phys. Rev. Lett.* **2003**, *90*, 4.
- [43] A. Walsh, C. R. A. Catlow, A. G. H. Smith, A. A. Sokol, S. M. Woodley, *Phys. Rev. B: Condens. Matter Mater. Phys.* **2011**, *83*, 220301.
- [44] K. Gömann, G. Borchardt, M. Schulz, A. Gömann, W. Maus-Friedrichs, B. Lesage, O. Kaitasov, S. Hoffmann-Eifert, T. Schneller, *Phys. Chem. Chem. Phys.* **2005**, *7*, 2053.
- [45] V. Metlenko, A. H. H. Ramadan, F. Gunkel, H. Du, H. Schraknepper, S. Hoffmann-Eifert, R. Dittmann, R. Waser, R. A. De Souza, *Nanoscale* **2014**, *6*, 12864.
- [46] S. P. Waldow, R. A. De Souza, *ACS Appl. Mater. Interfaces* **2016**, *8*, 12246.
- [47] R. A. De Souza, V. Metlenko, D. Park, T. E. Weirich, *Phys. Rev. B: Condens. Matter Mater. Phys.* **2012**, *85*, 174109.
- [48] B. Rahmati, J. Fleig, W. Sigle, E. Bischoff, J. Maier, M. Rühle, *Surf. Sci.* **2005**, *595*, 115.
- [49] T. Heisig, C. Baeumer, U. N. Gries, M. P. Mueller, C. La Torre, M. Luebben, N. Raab, H. Du, S. Menzel, D. N. Mueller, C. L. Jia, J. Mayer, R. Waser, I. Valov, R. A. De Souza, R. Dittmann, *Adv. Mater.* **2018**, *30*, 1800957.
- [50] C. Baeumer, C. Schmitz, A. Marchewka, D. N. Mueller, R. Valenta, J. Hackl, N. Raab, S. P. Rogers, M. I. Khan, S. Nemsak, M. Shim, S. Menzel, C. M. Schneider, R. Waser, R. Dittmann, *Nat. Commun.* **2016**, *7*, 12398.
- [51] C. Baeumer, C. Funck, A. Locatelli, T. O. Menteş, F. Genuzio, T. Heisig, F. Hensling, N. Raab, C. M. Schneider, S. Menzel, R. Waser, R. Dittmann, *Nano Lett.* **2019**, *19*, 54.
- [52] M. Luysberg, M. Heggen, K. Tillmann, *J. large-scale Res. Facil.* **2016**, *2*, 77.
- [53] A. Pedone, G. Malavasi, M. C. Menziani, A. N. Cormack, U. Segre, *J. Phys. Chem. B* **2006**, *110*, 11780.
- [54] S. Plimpton, *J. Comput. Phys.* **1995**, *117*, 1.
- [55] T. O. Menteş, G. Zamborlini, A. Sala, A. Locatelli, *Beilstein J. Nanotechnol.* **2014**, *5*, 1873.
- [56] H. Kim, O. Renault, A. Tyurnina, J. P. Simonato, D. Rouchon, D. Mariolle, N. Chevalier, J. Dijon, *Appl. Phys. Lett.* **2014**, *105*, 011605.